Second harmonic generation and crystal structure of a self-assembled Boc-p-nitro-L-phenylalanyl-p-nitro-l-phenylalanine dipeptide †

Rosa M. F. Baptista, © ¿ [a] Alejandro P. Ayala, © [b] Etelvina de Matos Gomes, (iD) [a] M. Cidália R. Castro, [c] Ana V. Machado [c] and Michael S. Belsley (iD) [a]

Abstract

(Boc ¿ tert-butoxycarbonyl)-p-nitro-l-phenylalanyl-p-nitro-l-phenylalanine, a dipeptide characterised by acentric symmetry, self-assembles into microtapes. This study explores its thermal, structural, and nonlinear optical properties. Thermogravimetric Analysis reveals an onset degradation temperature of $190^{\circ}C$, with primary and secondary peaks at $202^{\circ}C$ and $220^{\circ}C$, respectively. The crystal structure of the dipeptide was determined through single crystal X-ray diffraction at 100 K , confirming its crystallisation in a monoclinic crystal lattice, space group P2 with two molecules per unit cell. Additionally, optical second harmonic generation polarimetry indicates a nonlinear optical response, with an effective coefficient (d_{eff}) estimated to be at least $0.67\ pmV^{-1}$. This value is only four times lower than that of a state-of-the-art phasematched oriented β-barium borate nonlinear crystal. The crystal is unusually robust against optical damage for an organic crystal, underlining the potential of this dipeptide in nonlinear optical applications.

Introduction

Novel organic materials derived from molecular self-assembly through low-energy interactions, such as van der Waals forces, electrostatic interactions, hydrogen bonds, and $\pi-\pi$ stacking, give rise to well-ordered supramolecular structures. Selfassembled peptide-based systems offer a versatile method for creating nanostructured materials using amino acids as natural building blocks. These systems are attracting increasing attention due to their biocompatibility and diverse structural and functional properties, with applications ranging from regenerative medicine to fluorescent probes, light energy

harvesting, and optical waveguiding. [1–4] The spontaneous selforganization process of peptide nanostructures provides a significant advantage over other organic materials.

Second harmonic generation (SHG) has proven to be a valuable tool for investigating the structures of peptide systems. Brevet and collaborators have extensively studied the nonlinear optical responses of specific peptides, particularly in solutions and at interfaces. [5,6]

There are few published articles on the second harmonic response of peptide crystals in the solid phase. Handelman et al. measured the effective second harmonic nonlinear susceptibility (d_{eff}) of diphenylalanine nanotubes and triphenylalanine nanobelts in reflection, reporting values of 12 pmV^{-1} and 0.34 pmV^{-1} respectively. [7] Although they did not determine the corresponding crystalline structures, second harmonic polarimetry suggested that the diphenylalanine nanotubes likely crystallised in a structure with six-fold symmetry. More recently Nandi et al. [8] demonstrated that in peptides containing coumarin, the variation of second harmonic intensity with incident laser polarisation strongly correlated with crystal packing. However, they did not estimate the effective nonlinear susceptibility.

Aromatic and aliphatic dipeptide nanotubes (NTs) represent a unique class of bio-inspired nanostructures, forming simple and modifiable organic materials that crystallise into tubular structures hundreds of nanometers long with internal diameters of tens of angstroms. These structures result from the stacking of molecules through intermolecular hydrogen bonds between functional groups in the peptide backbone. [9,10]

Among these self-assembling systems, l-phenylalanyl-lphenylalanine, or diphenylalanine (PhePhe) is the most extensively studied. [11] PhePhe self-assembles into NTs with large hydrophilic channels, as revealed by Gorbitz, [12] and can form nanowires [13] and nanorods [14] depending on experimental conditions such as pH and temperature. Structurally, due to the chirality of l-phenylalanine amino acid, PhePhe NTs form noncentrosymmetric structures that crystallise in the $P6_{1,5}$ space group. [12]

The physical properties of PhePhe have been characterised through various methods. First-principles calculations have determined an energy bandgap of 4.48 eV for self-assembled Phe-Phe, classifying the dipeptide as a wide bandgap semiconductor. [15]

Mechanically, these nanostructures exhibit extraordinary properties, with a high average point stiffness of 160 $N\ m^{-1}$ and a Young's modulus of $19-27\,GPa$, placing them among the stiffest known biological materials. [16] An effective nonlinear optical coefficient $d_{\text{eff}} = 12\ pmV^{-1}$, has been reported for PhePhe NTs. [7] However, this nonlinearity is one order of magnitude smaller than that of the state-of-the-art organic crystal 2-methyl-4-nitroaniline (MNA). [17] PhePhe NTs have been integrated into devices for electronic and biosensing applications. [18–20]

The PhePhe dipeptide structural family has been expanded to include several analogues. One such analogue is the aminemodified Boc-l-phenylalanyl-l-phenylalanine (hereafter BocPhePhe, Boc ¿ tert-butoxycarbonyl) which forms various nanoscale structures such as nanospheres (NS) [21] and NTs. [22] Another significant analogue is Boc- p-nitro- L -phenylalanyl- p -nitro-l-phenylalanine (Boc- p NPhepNPhe) notable as the first

dipeptide reported displaying dual self-assembly from 1,1,1,3,3,3-hexafluoro-2-propanol (HFP) and water solutions, forming microtapes composed of self-assembled nanotubes. [23]

Across these dipeptide systems directional intermolecular $\pi-\pi$ interactions and hydrogen-bonding networks give rise to quantum confined (QC) structures (that is, nanocrystalline regions possessing strong QC properties) exhibiting pronounced exciton effects. [24–26] Comparative optical absorption measurements show that the self-assembled Boc- *p* NPhepNPhe dipeptide has a maximum absorption at $270\ nm$, [23] which corresponds to an energy bandgap of 4.6 eV , similar to the 4.4 eV reported for self-assembled PhePhe dipeptide. [27,28]

All amino acids, except glycine, naturally possess a chiral molecular structure and consequently, crystallise without a centre of symmetry. This lack of a centre of symmetry enables properties such as piezoelectricity and optical second harmonic generation in crystalline compounds. As a result, dipeptides formed from chiral l-phenylalanine amino acid or its derivatives, are non-centrosymmetric bio-active systems ideal for exploring these properties. Recently, the piezoelectric properties of self-assembled Boc- *p* NPhepNPhe, Fig. 1, when embedded into electrospun polymer fibres have been reported, demonstrating a strong piezoelectric response to an applied periodical deformation. [23]

While the molecular self-assembly of these diphenylalanine derivatives has been extensively studied, the solid-state crystalline structure is known only for the Boc-PhePhe dipeptide. In this work, we report the crystal structure of Boc-

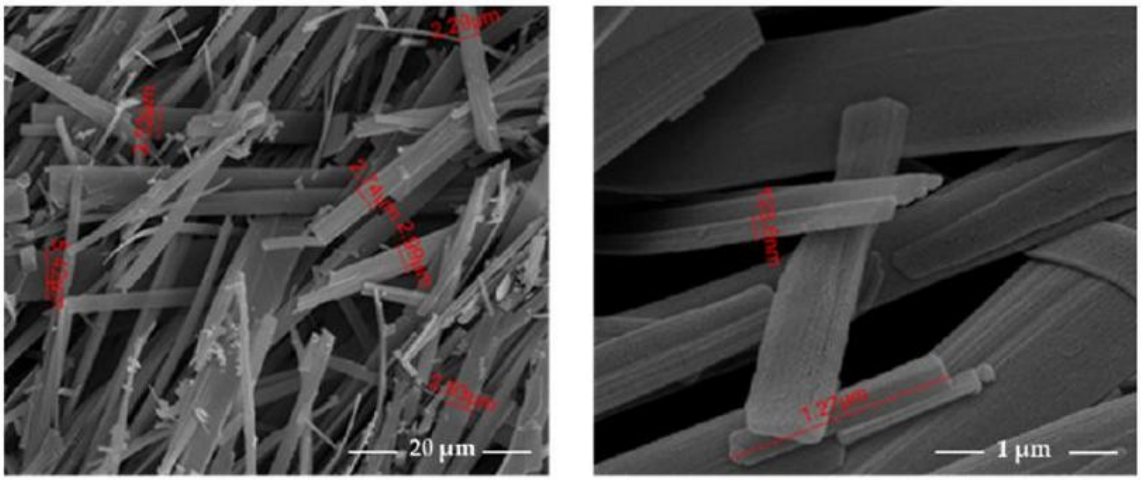

Fig. 1 SEM images of Boc- *p*-nitro-L-phenylalanyl- *p*-nitro-Lphenylalanine (Boc ¿ tert-butoxycarbonyl) dipeptide crystals at 5000 × and 100000 × magnifications (reproduced with permission from ref. 23).

p NPhepNPhe determined by single crystal X-ray diffraction at 100 K. Furthermore, given the acentric nature of the crystal space group, we investigate the optical second harmonic generation (SHG) properties of Boc- *p* NPhepNPhe microtapes.

Experimental section

Materials and synthesis

p-Nitro-L-phenylalanine (pNPhe), 1-hydroxybenzotriazole (HOBt), *N* ,*N*-dicyclohexylcarbodiimide (DCC), thionyl chloride, and di-tert-butylpyrocarbonate (Boc_2O) were purchased from SigmaAldrich or Alfa Aesar and used without further purification. All solvents were purchased from Sigma-Aldrich and used as received.

The synthesis began by protecting the acid terminal of *p* NPhe through a reaction with thionyl chloride in methanol, yielding the corresponding methyl ester of the amino acid. Then, the amino terminal was protected by a reaction with di-tert-butylpyrocarbonate, resulting in the *N*-Boc-protected amino acid. The dipeptide was obtained by liquid-phase synthesis, coupling the amino acid methyl ester with the *N*-Boc-protected amino acid, using DCC/HOBt as coupling agents.

Further details of the synthesis can be found in the previously published article [23] where the Raman spectra of the Boc- *p* NPhepNPhe was also reported.

Differential Scanning Calorimetry (DSC) and Thermogravimetric Analysis (TGA)

Differential Scanning Calorimetry (DSC) analysis was performed in a Netzsch 200 Maya (Netzsch, Selb, Germany) under nitrogen flow ($50\ \ mL\ \ min^{-1}$). The sample was placed in an aluminium pan. Two heating and one cooling ramp were run at: $2\ \ K\ \ min^{-1}$, from: $-30^{\circ}C$ to $200^{\circ}C$. Thermogravimetric Analysis (TGA) was performed using a TA Q500 thermogravimetric analyser (TA Instruments, New Castle, DE, USA). The sample was placed in a platinum crucible and heated from $30^{\circ}C$ to $700^{\circ}C$ at a heating rate of $10^{\circ}C\ min^{-1}$ under a nitrogen flow ($60\ \ mL\ \ min^{-1}$).

Single-crystal X-ray diffraction

Single-crystal X-ray diffraction data (φ scans and ω scans with κ and θ offsets) were collected on a Bruker D8 Venture diffractometer configured in κ-geometry, equipped with a

Photon II CPAD detector and an I μ S 3.0 Incoatec microfocus source *CuK* α ¿ Å). A suitable crystal was selected and mounted on a Kapton fibre using a MiTeGen MicroMount with immersion oil. Data collection was performed at 100 K with an Oxford Cryostream cryostat (800 series Cryostream Plus) attached to the diffractometer. The APEX 4 software [29] was used for unit cell determination and data collection. Data reduction and global cell refinement were carried out with the Bruker SAINT+ software package, [30] and an absorption correction was applied using a multi-scan method via SADABS. [31] The structure was solved through intrinsic phasing using ShelXT (Sheldrick, 2015) [32] within the Olex2 interface [33] to the SHELX suite, allowing the location of most

non-hydrogen atoms. The remaining non-hydrogen atoms were identified from Fourier difference maps calculated through successive full-matrix least-squares refinement cycles on F^2 using ShelXL [32] and refined with anisotropic displacement parameters. Hydrogen atoms were placed geometrically and refined using the riding model. Artwork representations were prepared using MERCURY [34] and PLATON. [35] The crystallographic data reported here are available under accession number CCDC: 2391827. Tables and the CIF file were generated using FinalCif. [36]

Second harmonic generation

The second harmonic signals were obtained using a modelocked Ti:sapphire oscillator (Coherent Mira) with a nominal pulse duration of 100 fs running at a repetition rate of 76 MHz . Details of the experimental setup have been described previously. [37] Briefly, a combination half-wave plate and polariser was employed to control the incident power onto the samples. The incident beam was focused using a $\times 10$ microscope objective with a numerical aperture of 0.25 and an effective focal length of 16.5 mm , producing a spot of approximately $4\,\mu\ m\left(1/e^2\right)$ diameter in the focal plane. The resulting second harmonic signal in transmission was collected using a second objective ($\times 20$ with a numerical aperture of 0.4), filtered by a dichroic mirror, and then passed through a combination zero-order half-wave plate and fixed calcite polariser, before being filtered using a low-pass cut-off filter with a transition wavelength of 650 nm and focused into a multimode fibre bundle. At the output of the fibre bundle, a 0.3 m imaging spectrometer (Shamrock 303i form Andor) isolated the second harmonic signal around 400 nm . A cooled CCD camera (Newton 920 from Andor) was employed to capture the signal during a set integration time. Subsequently, the area under the approximately Gaussian second harmonic spectra was numerically integrated to provide the total number of detected photo-electrons during the integration window.

Before the focusing objective and after the collimating objective zero-order half-wave plates at 800 nm and 400 nm respectively were used to control the incident and detected linear polarisation states. Two different polarisation curves are presented " $q-p$ " and " $q-s$ ". The " $q-p$ " curve corresponds

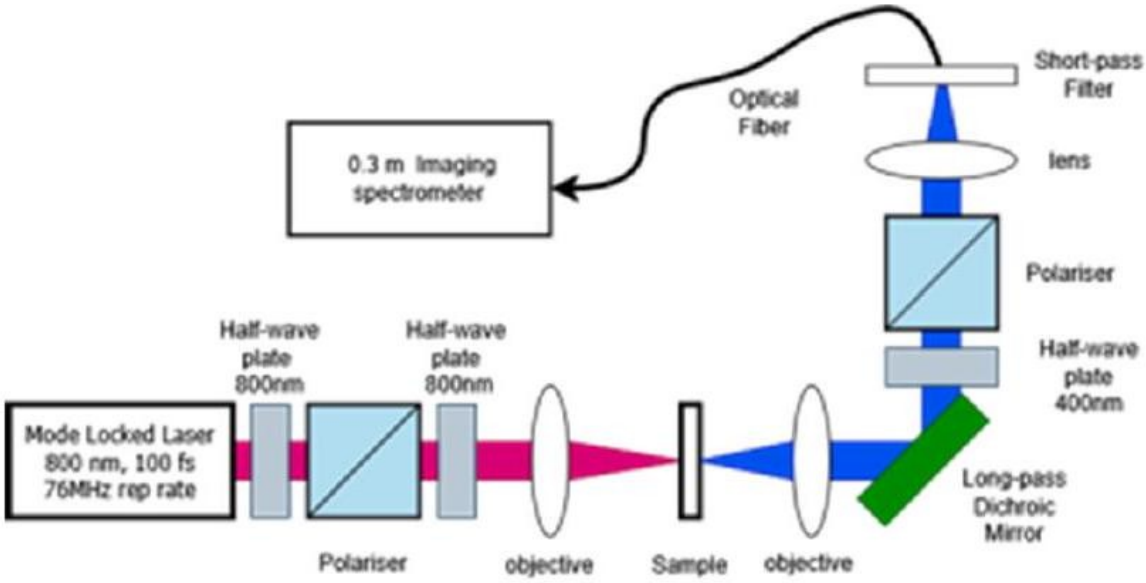

Fig. 2 Second harmonic measurement scheme.

to the case when the transmitted polarisation is that which gives rise to the maximum second harmonic signal. The halfwave plate before the focusing objective is then rotated to vary the fundamental polarisation of the incident light. For the " $q-s$ " the transmitted linear polarisation state was set orthogonal to the " $q-p$ " orientation and again the incident linear polarisation was varied using the half-wave plate (Fig. 2).

Results and discussion

Crystal structure of Boc- *p* NPhPNPhe

Boc- *p* NPhepNPhe crystallizes in the monoclinic crystal system, specifically in the non-centrosymmetric space group P2 (Table 1). The unit cell parameters are $a=12.4892(3)$ Å, b ¿5.11310(10) Å, $c=18.7509(4)$ Å, and $\beta=90.4730$ ¿. The

Table 1 Crystal data and structure refinement for Boc-pNPhepNPhe

CCDC number	2391827
Empirical formula	$C_{23}H_{26}\ N_4O_9$
Formula weight	502.48
Temperature [K]	100.00
Crystal system	Monoclinic
Space group (number)	P2 (3)
a[Å]	12.4892(3)

$b[\text{Å}]$	5.11310(10)
$c[\text{Å}]$	18.7509(4)
$\beta[^{\circ}]$	90.4730(10)
Volume [Å^3]	1197.36(5)
Z	2
$\rho_{\text{calc}}\left[g\,cm^{-3}\right]$	1.394
$\mu\left[mm^{-1}\right]$	0.921
$F(000)$	528
Crystal size [mm^3]	$0.026 \times 0.043 \times 0.443$
Crystal colour	Clear light colourless
Crystal shape	Needle
Radiation	$CuK_{\alpha}(\lambda = 1.54178\ \ A)$
2θ range [$^{\circ}$]	7.08 to 144.49¿ Å ¿
Reflections collected	52422
Independent reflections	$4670, R_{\text{int}} = 0.0772, R_{\text{sigma}} = 0.0315$
Data/restraints/parameters	4670/1/328
Goodness-of-fit on F^2	1.018
Final R indexes $[I \geq 2\sigma(I)]$	$R_1 = 0.0357, wR_2 = 0.0870$
Final R indexes [all data]	$R_1 = 0.0427, wR_2 = 0.0927$
Largest peak/hole [e Å-3]	0.25/-0.24
Flack X parameter	-0.06(9)

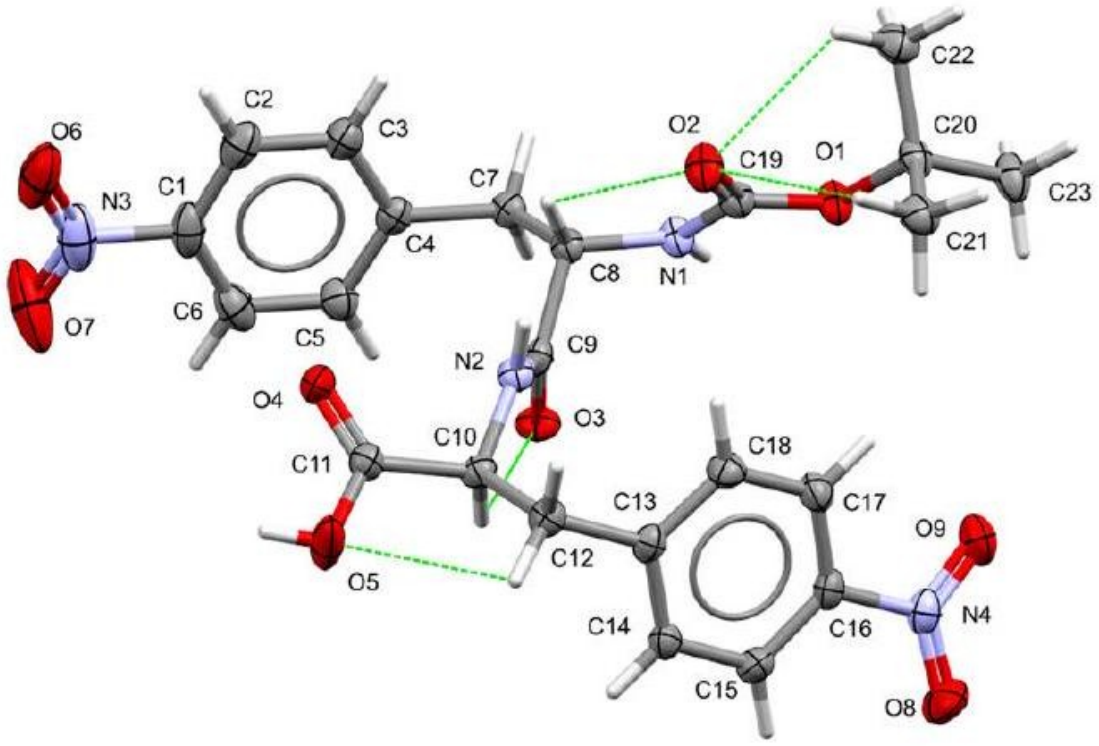

Fig. 3 Boc-pNPhepNPhe dipeptide asymmetric cell. Green dashed lines represent intramolecular hydrogen bonds.

asymmetric unit contains a single molecule, as illustrated in Fig. 3. Despite possessing bonds that allow significant conformational flexibility, the molecular conformation of Boc- *p* NPhepNPhe in the crystalline state is stabilized by a network of intramolecular hydrogen bonds, depicted as green dashed lines in Fig. 3. Furthermore, the near-zero value of the Flack parameter confirms that the absolute configuration was properly determined.

Notably, the intramolecular hydrogen bonds $C8-H8\cdots O2$ with a distance of $2.773(3)$ Å and $C10-H10\cdots O3$ at $2.806(3)$ Å are among the strongest in Boc- *p* NPhe *p* NPhe, playing a critical role in defining its molecular conformation. Despite these constraints, a geometry check performed using the Mogul routine [38] from the Cambridge Structural Database revealed no geometrical parameters significantly deviating from average values.

The predominant feature in the crystal packing of Boc *p* NPhe *p* NPhe is the formation of a dimer through a homosynthon interaction between the carboxylic groups, creating an $R_2^2(8)$ motif centred around the 2 -fold axis, as observed in the ac-projection of the crystal structure shown in Fig. 4a). This dimer is stabilised by a strong $O5-H5\cdots O4$ hydrogen bond, with its parameters listed in Table 2. The relative orientation of the molecules within the dimer is further defined by a weak hydrogen bond, $C14-H14\ \ A\cdots O7$, which together with the strong hydrogen bond determines the final geometry of the dimer.

The stacking of the strongly bonded dimers along the *b*-axis is facilitated by the trans configuration of the two amide moieties. This arrangement allows the formation of

infinite chains through strong $N1-H1\cdots O2$ and $N2-H2\cdots O3$ hydrogen bonds, as illustrated in the *bc*-projection of the structure depicted in Fig. 4b). These chains are further stabilised by two $\pi-\pi$ interactions between rings of the same type (4.7127 (15) Å), as well as by the weak hydrogen bond C5-H5A...O4.

Hydrogen bonds do not play a key role in the packing of the amide chains, as only the hydrogen bond ($C2-H2\ A\cdots O8$) links laterally dimers from consecutive layers. To gain a more comprehensive understanding of the crystal packing, we performed Hirshfeld surface (HS) analysis mapped with the

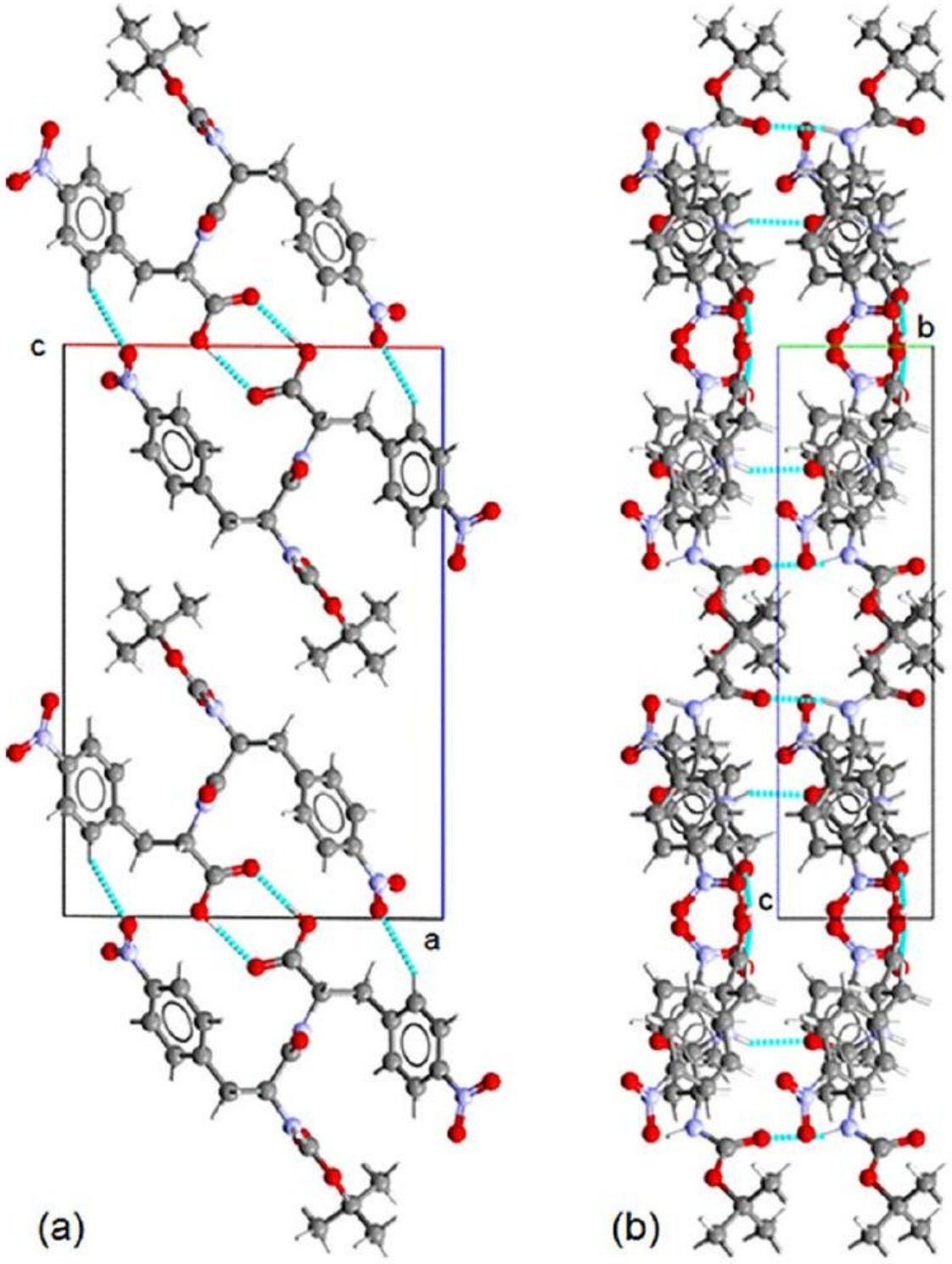

Fig. 4 Projections of the crystalline structure of the BocpNPhepNPhe: (a) ac-plane and (b) bc-plane.

shape index and generated two-dimensional fingerprint (2DF) plots using the CrystalExplorer software. [39] Mapping the HS with the shape index allows for the identification and visualization of specific intermolecular interactions, such as $\pi-\pi$ and

$X-Y\cdots\pi$ interactions, by highlighting complementary regions on the molecular surface. The 2DF plots condense this information into graphical representations that map the frequency and nature of contact points between molecules. These analytical tools are invaluable for comparing and clustering structures, identifying structural similarities, and extracting relevant information about intermolecular interactions. [40–42]

The HS and 2DF plots are presented in Fig. 5, where the regions above the aromatic rings are labelled (1) and (2). Notably, the characteristic red and blue triangles forming a

Table 2 Intermolecular hydrogen bond parameters for BocpNPhepNPhe (distances in Å and angles in ˚)

$D-H\cdots A$	$d(H\cdots A)$	$d(D\cdots A)$	<(DHA)
$O5-H5\cdots O4^{¿1}$	1.83	2.625(3)	158
$N1-H1\cdots O2^{¿2}$	2.09	2.935(3)	162
$N2-H2\cdots O3^{¿3}$	2.09	2.892(3)	151
$C2-H2\ \ A\cdots O_8{}^{¿4}$	2.42	3.089(4)	129
$C5-H5\ \ A\cdots O4^{¿2}$	2.53	3.286(4)	136
$C14-H14\ \ A\cdots O_7{}^{¿1}$	2.49	3.350(4)	151

Symmetry transformations used to generate equivalent atoms: #1: 1 $x,y,-z;¿2:x,-1+y,z;¿3:x,1+y,z;¿4:1+x,1+y,z.$

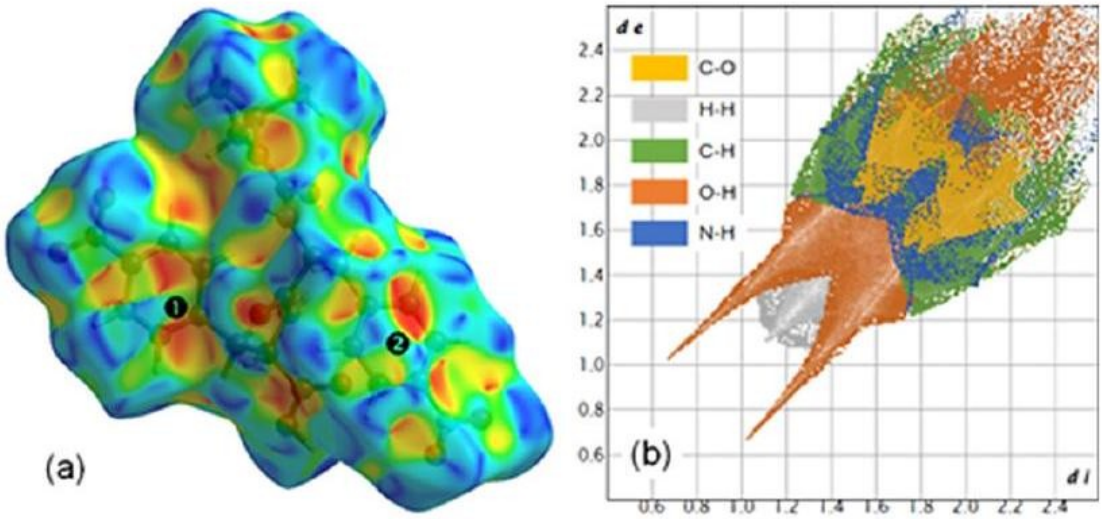

Fig. 5 (a) Hirshfeld surface of Boc-pNPhepNPhe mapped with the shape index, with labels 1 and 2 highlighting regions over the aromatic rings. (b) Corresponding 2D fingerprint plot; the colour coding of distance pair frequencies includes reciprocal

contacts.
'bow-tie' pattern over the ring (1) highlight the $\pi-\pi$ interactions associated with the dimer stacking of the amide chains (Fig. 5a). Above the ring (2), the HS mapping is less defined, displaying two diffuse 'bow-tie' patterns related to two $\pi-\pi$ bonds: one associated with the stacking and a stronger interaction (4.7127(15) Å) between rings of different types, which contributes to the packing of the chains. In this region, a red depression indicates the N4-O8 $\cdots\pi$ interaction (3.449)(3) Å), is also contributing to the alignment of the parallel chains. This latter interaction is observable in the 2DF plot through the frequency of the C-O distances, which exhibit the wing-like pattern commonly associated with $C-H\cdots\pi$ interactions (Fig. 5b). Finally, it is noteworthy that the 2 DF plot is dominated by two strong spikes corresponding to $O-H$ distances, highlighting the key role of the carboxylic-carboxylic and amide-amide interactions in forming and stacking the Boc- *p* NPhe *p* NPhe dimers.

Differential Scanning Calorimetry (DSC) and Thermogravimetric Analysis (TGA)

To examine the thermal stability and check for the existence of structural phase transitions of Boc- *p* NPhepNPhe dipeptide, Differential Scanning Calorimetry (DSC) and Thermogravimetric Analysis (TGA) were performed. Fig. 6a) and b) present thermographs of dipeptide microtapes, illustrating thermal transitions and weight loss, respectively. TGA shows an onset temperature (T_{onset}) at $190^{\circ}C$, with a primary degradation peak at $202^{\circ}C$ followed by a secondary one at $220^{\circ}C$, attributed to the degradation of the crystalline compound, Fig. 6a). This is also observed in the first heating cycle of the DSC analysis, Fig. 6b). The total weight loss recorded is 35%. A final degradation stage is identified at $315^{\circ}C$ accompanied by a further decrease in weight of 20%. The second heating curve in Fig. 6b) is consistent with the full degradation of the compound. There are no reversible phase transitions that could indicate any crystal structural changes, with temperature.

Optical second harmonic generation

Second harmonic generation (SHG) is a nonlinear optical process, where a fundamental wave of frequency ω, incident

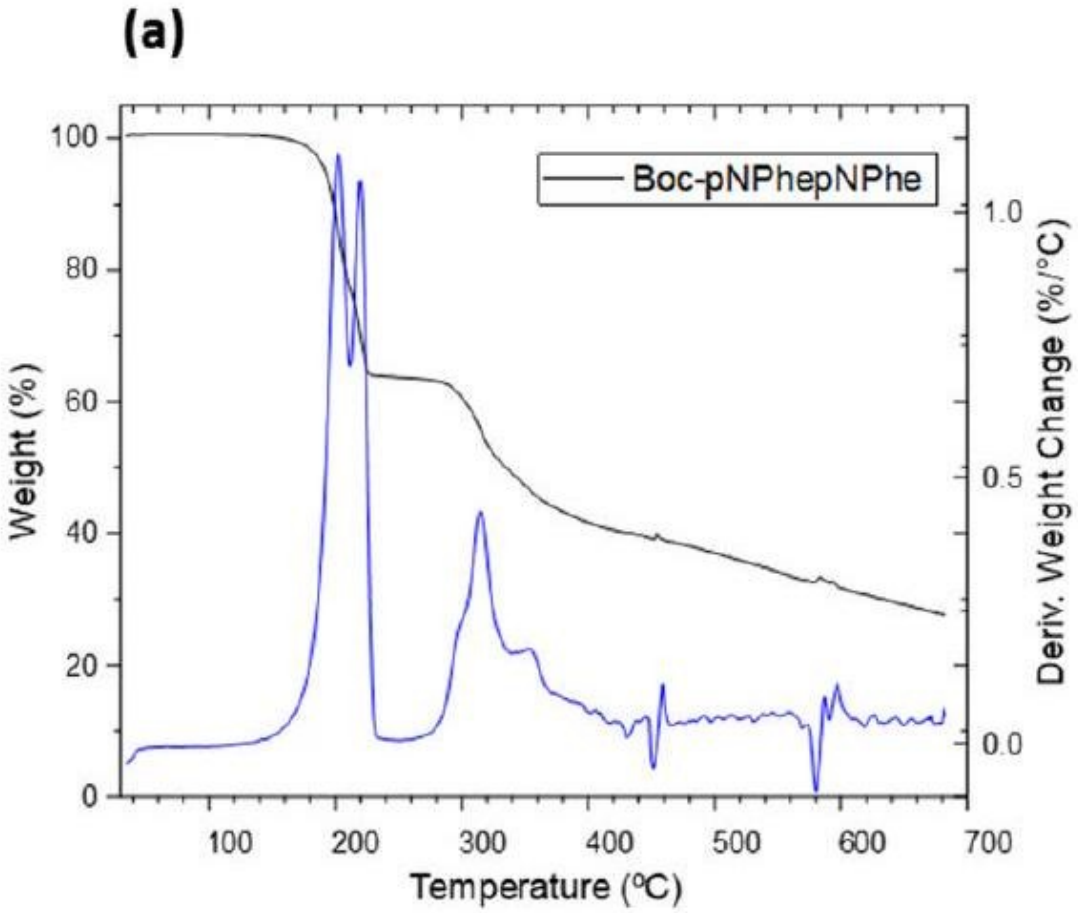
(a)
Boc-pNPhepNPhe
Weight (%)
Deriv. Weight Change (%/°C)
Temperature (°C)
100
80
60
40
20
0
1.0
0.5
0.0
100
200
300
400
500
600
700

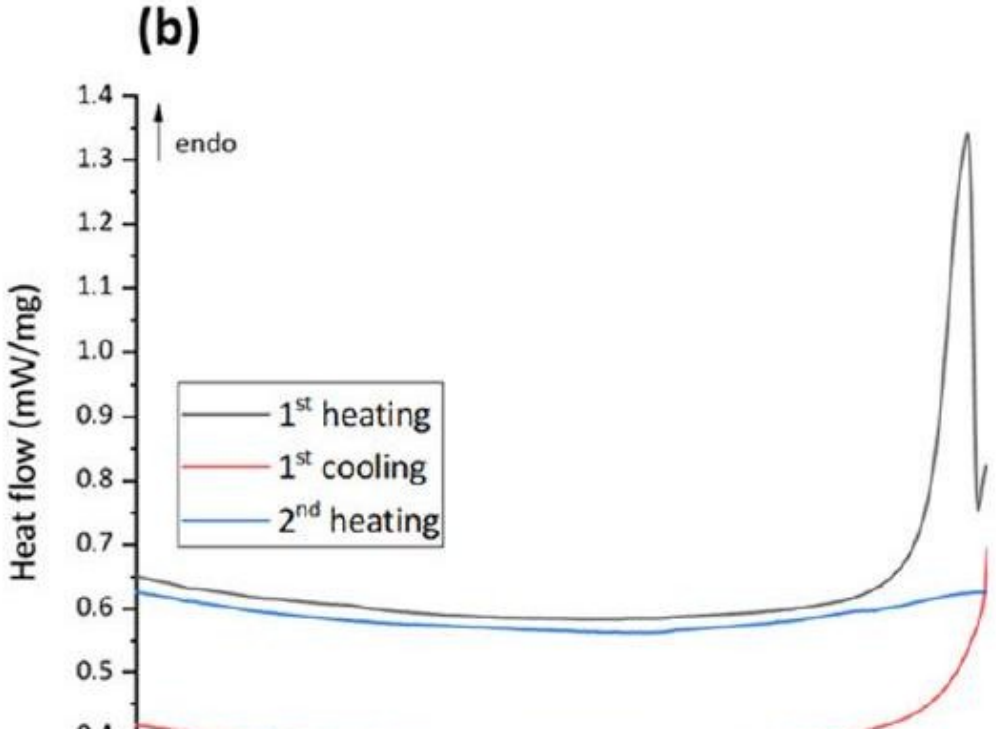
(b)
endo
Heat flow (mW/mg)
1st heating
1st cooling
2nd heating
1.4
1.3
1.2
1.1
1.0
0.9
0.8
0.7
0.6
0.5

Fig. 6 (a) Thermogravimetric Analysis (TGA) and (b) Differential Scanning Calorimetry (DSC) for Boc-pNPhepNPhe dipeptide crystal tapes.

on an acentric crystalline medium, generates another optical wave of frequency 2ω, due to the nonlinear polarisation of the medium. Biological materials such as proteins, collagen and viruses, are known to exhibit SHG phenomena due to their non-centrosymmetric structures. [43] This property is described by a 3rd-rank tensor, where the tensor elements are determined by the crystal point group symmetry. [44] Although SHG has been studied in detail for several organic crystals, very few studies have been reported on dipeptide crystals.

In this work we measure SHG on Boc- *p* NPhepNPhe crystal microtapes, which belong to crystallographic point group 2, the crystals are therefore biaxial. Assuming Kleinman symmetry, the second harmonic light polarisation for this point group takes the general form:

$$\begin{bmatrix} P_1^{2\omega} \\ P_2^{2\omega} \\ P_3^{2\omega} \end{bmatrix} = \begin{bmatrix} 0 & 0 & 0 & d_{14} & 0 & d_{21} \\ d_{21} & d_{22} & d_{23} & 0 & d_{14} & 0 \\ 0 & 0 & 0 & d_{23} & 0 & d_{14} \end{bmatrix} \begin{bmatrix} E_1^{\omega} E_1^{\omega} \\ E_2^{\omega} E_2^{\omega} \\ E_3^{\omega} E_3^{\omega} \\ 2E_2^{\omega} E_3^{\omega} \\ 2E_1^{\omega} E_3^{\omega} \\ 2E_1^{\omega} E_2^{\omega} \end{bmatrix} \quad (1)$$

Here E_1, E_2 and E_3 (1,2,3 refer to the dielectric crystal axis x, y, z respectively) are the electric fields associated with the fundamental optical wave; $P_1^{2\omega}, P_2^{2\omega}, P_3^{2\omega}$ are the nonlinear polarizations generated inside the medium and $d_{ij} i, j = 1,2,3$ are the non-linear optical crystal coefficients. In Fig. 7 the

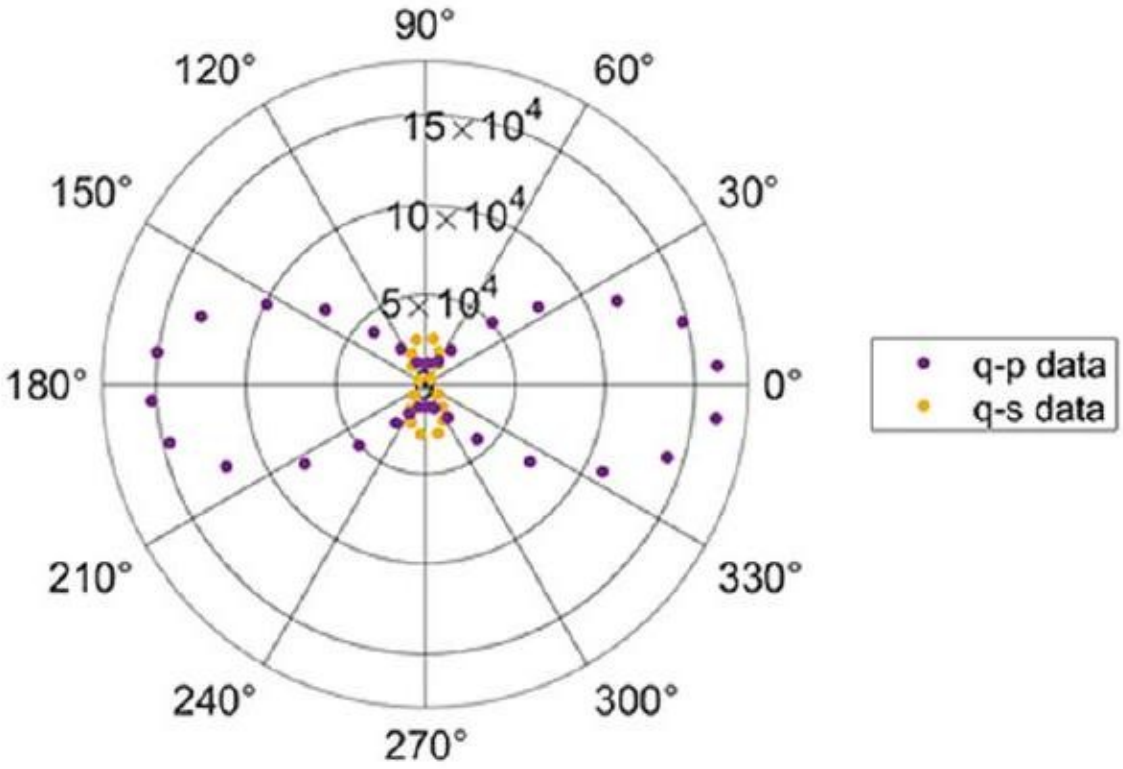

Fig. 7 The second harmonic signal generated by Boc-pNPhepNPhe crystal microtapes as a function of the orientation of the fundamental beam's polarisation orientation relative to the transmission axis of the analyser.

second harmonic polarimetry curves for a Boc- p NPhepNPhe crystal are plotted. For the $q-p$ curve, the analyser was oriented along the direction of the strongest second harmonic response, while for the $q-s$ curve the analyser was aligned perpendicular to that direction. In both curves, the angle q represents the orientation of the incident linear polarisation. The incident fundamental optical wave vector was perpendicular to the crystallographic b-axis which lies in the plane of the microtapes and is assigned to the dielectric y-axis Due to the difficulty in growing large optically uniform crystals it was not possible to determine the x and z dielectric axes relatively to the crystallographic axes. However, the incident wavevector must lie in the dielectric $x-z$ plane. We assume k propagates at an angle θ relative to the dielectric z-axis, i.e. $k=k\sin(\theta)\acute{x}+k\cos(\theta)\acute{z}$. Neglecting any effects of spatial walk-off, the incident electric field polarization will have components perpendicular to this wavevector,

$$\begin{bmatrix} E_1^{\omega} \\ E_2^{\omega} \\ E_3^{\omega} \end{bmatrix} = E^{\omega} \begin{bmatrix} \cos(\theta)\sin(q) \\ \cos(q) \\ -\sin(\theta)\sin(q) \end{bmatrix} \quad (2)$$

Here we have taken the reference of the incident polarization orientation, $q=0$, to be along the axis of major symmetry, i.e. the dielectric y-axis or the crystallographic b-axis. This gives rise to the following second harmonic nonlinear polarizations,

dielectric y-axis is dominant and we can model the generated second harmonic intensity as

$$I^{2\omega} \propto \left(I^{\omega}\right)^2 \left(d_{22}\right)^2 \cos^4\left(q\right) \quad (4)$$

The Boc p NPhe p NPhe micro tapes $q-p$ curve in Fig. 7 is very nearly a pure $\cos^4\left(q\right)$ dependence, suggesting that the second harmonic response of a crystalline material is dominated by the d_{22} tensor element. However, the $q-p$ curve does not completely go to zero at 90 and 270 degrees. A possible explanation is that the microtapes are themselves self-assembled from a collection of nanorods. Domain boundaries, defects, inhomogeneities or the presence of small surface inclusions with a different orientation from the main illuminated microtape might lead to a small orthogonally polarised contribution to second harmonic light as observed. We obtain an excellent fit to the experimental data assuming a small orthogonal contribution added in quadrature to the dominate term. Fig. 8 shows the fit to the $q-p$ curve by a function of the form. $\left[A\cos^4\left(\theta\right)+B\sin^4\left(\theta\right)\right]$ with $A=\left(1.62\pm0.01\right)\times10^5$ counts and $B=\left(1.3\pm0.1\right)\times10^4$ counts.

To estimate the effective second-order nonlinear susceptibility, d_{eff} , which, in line with the above arguments, is dominated by the d_{22} tensor element, we calibrated our measurements using a reference nonlinear crystal. The efficiency of our experimental set-up. We employed a 1 mm thick BBO crystal (barium beta borate, EKSMA) phasematched for an 800 nm fundamental wavelength. Under the strong focusing conditions of our $\times10$ microscope objective, the effective interaction length for second harmonic generation in the BBO crystal was approximately $30\,\mu\ m$, limited by the 68 milliradian spatial walk-off angle of the second harmonic light. The calibration procedure followed our previously published methodology [45] with the key points summarised in the supplementary information. Table 3 presents the relevant experimental parameters and quantitative results. Notably, the measurements from the Boc- p NPhepNPhe microtapes were conducted at normal incidence without optimization of the fundamental beam's angle of incidence. Consequently, the reported d_{eff} value represents a lower bound estimate of the material's nonlinear optical response, which could potentially be enhanced through angular optimization.

$$\begin{bmatrix} P_1^{2\omega} \\ P_2^{2\omega} \\ P_3^{2\omega} \end{bmatrix} = E^{\omega 2} \begin{bmatrix} \left[d_{21}\cos\left(\theta\right)-d_{14}\sin\left(\theta\right)\right]\sin\left(2q\right) \\ d_{21}\cos^2\left(\theta\right)\sin^2\left(q\right)+d_{22}\cos^2\left(q\right)+d_{23}\sin^2\left(\theta\right)\sin^2\left(q\right)-d_{14}\sin\left(2\theta\right)\sin^2\left(q\right) \\ \left[d_{14}\cos\left(\theta\right)-d_{23}\sin\left(\theta\right)\right]\sin\left(2q\right) \end{bmatrix} \quad (3)$$

The second harmonic polar plots of Fig. 7 predominantly display a two-fold symmetry which suggests that, if the incident wavevector is perpendicular to the crystallographic b-axis, the terms proportional to $\sin\left(2q\right)$ are negligible, that is the tensor elements d_{14}, d_{21} and d_{23} are small compared to d_{22}. Consequently, the induced polarisation along the

Notably, the average incident intensity used to measure the second harmonic response of the dipeptide crystal was approximately $10\,GW\,cm^{-2}$ and no evidence of optical damage was seen after over 10^9 incident pulses. This implies that the Boc- p NPhepNPhe crystal

is unusually robust against optical damage for an organic crystal.

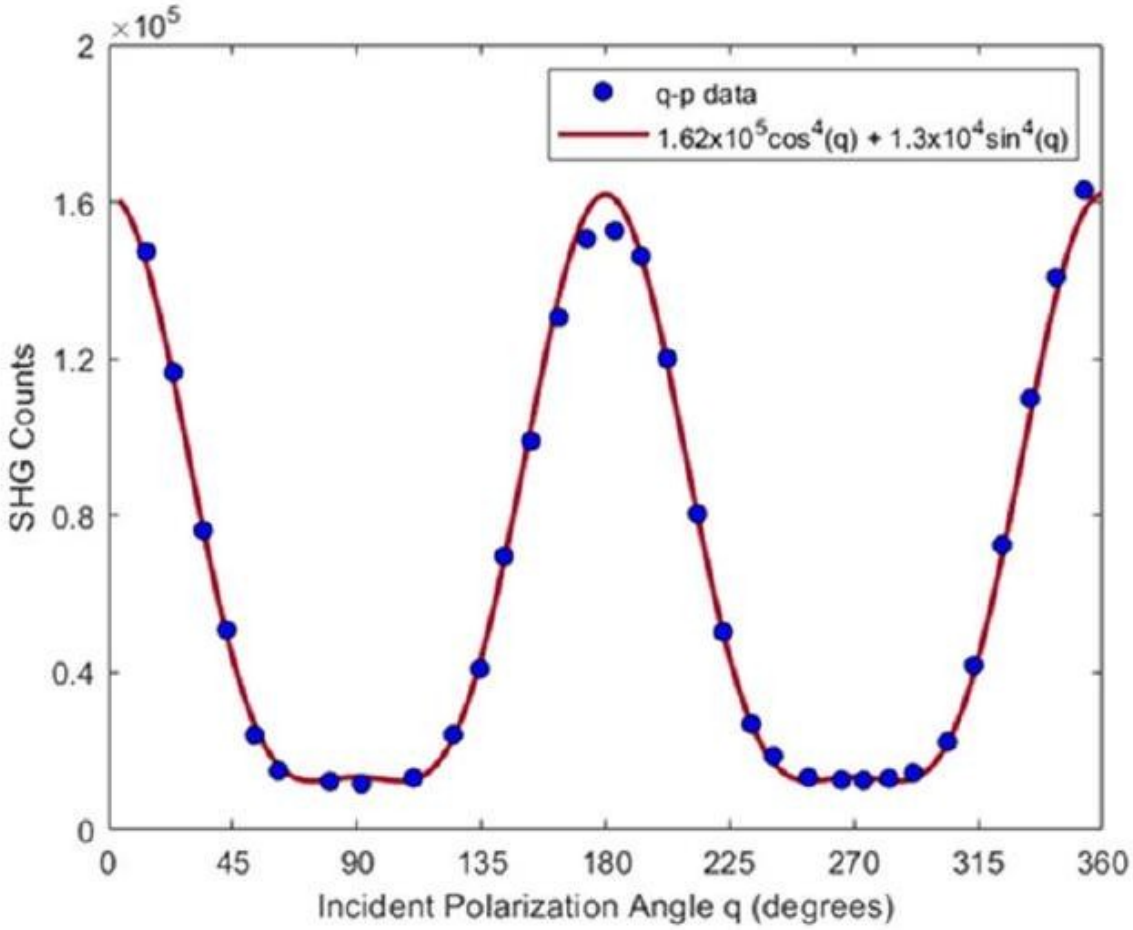

Fig. 8 The second harmonic response for the $q-p$ orientation, that is with the analyser aligned along the direction that gave rise to the largest detected second harmonic signal and polarisation of the incident fundamental beam's polarisation direction being rotated over 360°. Also shown is a theoretical fit corresponding to the model of eqn (4) with a small orthogonal component added as indicated in the legend.

Admittedly, our lower bound estimate is significantly smaller than the $12\ pm\ V^{-1}$ value reported by Handelman et al. for diphenylalanine (PhePhe) nanotubes. [7] At first glance, this discrepancy may seem surprising, given the presence of two strong electron-withdrawing nitro NO_2 groups in Boc$p$ NPhepNPhe. However, the electron interactions within the Boc- p NPhe p NPhe molecule are complex, owing to the interplay of multiple functional groups, including the nitro groups, the carboxylic acid group, and the bulky Boc protecting group. As illustrated by the Hirshfeld surface map in Fig. 5a, complex variations in the electronic charge distribution are visible. These variations arise from several factors: the steric hindrance introduced by the Boc group, which slightly misaligns the charge distribution of the two nitro groups, and the modification of the carboxylic acid group's effect on the overall dipole moment. This complex interplay of factors results in a somewhat higher dipole moment in one of the moieties containing the

Boc compared to the other, despite a significant cancellation between the local dipole moments associated with the two NO_2 groups.

Additionally, there are several other key factors which could contribute to this discrepancy between reported d_{eff} values. First, diphenylalanine crystallises in the highersymmetry P_6 space group, while Boc- p NPhepNPhe crystallises in the lower-symmetry P2 space group, with only two dipeptides per unit cell. Second, our lower estimate for Boc- p NPhepNPhe's d_{eff} exceeds the $0.34\ pm\,V^{-1}$ value reported by Handelman et al. for triphenylalanine nanobelts, [7]
which are morphologically more similar to the Boc p NPhepNPhe micro tapes and share the same point group 2. Moreover, as noted in ref. 7, diphenylalanine self-assembles into hexagonal-shaped nanotubes filled with water molecules, a structural feature likely to enhance its nonlinear optical properties.

Finally, Handelman et al. calibrated their measurements using a relatively high value of $0.8\ pm\,V^{-1}$ for the χ_{111} tensor element of z-cut quartz. Several references in the literature quote a lower value of $0.6\ pm\,V^{-1}$ [ref. 46 and 47 and references therein]. Moreover, Handelman's equation (6) used to describe the second harmonic response and calibrate their measurements is appropriate for normally incident plane waves generating second harmonic light in transmission, while their measurements were performed using a focused femtosecond laser incident at 45 degrees to the sample's surface.

In summary, while the reported nonlinear response of Boc p NPhepNPhe is smaller than that of diphenylalanine nanotubes, there are significant differences in the crystal symmetry, molecular packing, and experimental calibration methods. Taken together, these factors underscore the importance of both structural and experimental considerations in interpreting nonlinear optical measurements.

Conclusions

The dipeptide Boc- p NPhe p NPhe exhibits remarkable selfassembly properties, forming microtapes and crystallizing in the non-centrosymmetric space group $P2$ with two molecules in the asymmetric unit cell. Despite possessing bonds that allow significant conformational flexibility, the molecular conformation of Boc- p NPhepNPhe in the crystalline structure is stabilized by a network of intramolecular hydrogen bonds. Notably, $C8-H8\cdots O2$¿ Å) and $C10-H10\cdots O3$¿ Å) intramolecular hydrogen bonds play a fundamental role in determining the molecular conformation.

The crystal packing is characterized by the formation of dimers through homosynthon interactions between carboxylic groups, centered on the 2 -fold axis. These dimers further stack along the 2 -fold axis, forming chains along the b-axis through strong $N1-H1\cdots O2$ and $N2-H2\cdots O3$ hydrogen bonds.

Thermal analysis demonstrates the stability of the crystalline compound up to approximately $190^{\circ}C$, highlighting its robust nature.

The non-centrosymmetric crystal structure of Boc p NPhepNPhe enables nonlinear optical effects. Second harmonic generation measurements and calculations reveal a lower bound for the effective second-order nonlinear susceptibility coefficient

Table 3 Second harmonic generation parameters for Boc-pNPhepNPhe crystal microtapes

Single crystal	Fundamental wave average power (mW)	Signal integration time (ms)	Effective thickness (μm)	Second harmonic signal (counts)	d_{eff} $\left(pm\,V^{-1}\right)$
BBO	0.5	2.5	30	2.44×10^{6}	2.0
Boc-pNPhepNPhe	5	250	0.5	1.62×10^{5}	0.67

d_{eff} of $0.67\ pm\,V^{-1}$, comparable to the state-of-the-art phasematched BBO (barium beta borate) crystal. Boc-pNPhepNPhe dipeptide crystals are also robust against optical damage. These findings suggest that the Boc- $pNPhepNPhe$ dipeptide is a promising candidate for nonlinear optical applications.

In conclusion, the combined structural and optical properties of Boc- p NPhepNPhe make it a subject for further research in the fields of supramolecular chemistry and nonlinear optics, with potential applications in advanced photonic devices.

Data availability

All data supporting the findings of this study are included in the article and its ESI † files. The crystallographic data are available under accession number CCDC: 2391827.

Author contributions

Rosa M. F. Baptista and Etelvina de Matos Gomes conceived and coordinated all the work, analysed the results, and wrote and edited the manuscript. Michael S. Belsley supervised the experimental non-linear optical work and wrote and edited the manuscript. M. Cidália R. Castro and Ana V. Machado carried out the DSC and TGA analyses. Alejandro P. Ayala performed the single crystal X-ray structure determination, Hirshfeld analysis and wrote and edited the manuscript. All authors discussed and commented on the manuscript.

Conflicts of interest

There are no conflicts to declare.

Acknowledgements

This research was funded by Fundação para a Ciência e Tecnologia through FEDER (European Fund for Regional Development)-COMPETE-QREN-EU (ref. UID/FIS/04650/2013 and UID/FIS/04650/2019). Rosa M. F. Baptista acknowledges

for her contract DL57/2016, with reference DL 57/2016/CP1377/CT0064 (DOI: https://doi.org/10.54499/DL57/2016/CP1377/CT0064). The authors acknowledge Cesar Bernardo for collecting the nonlinear optical data.

References

1 H. Liu, J. Xu, Y. Li and Y. Li, Acc. Chem. Res., 2010, 43, 1496-1508.
2 O. Berger, L. Adler-Abramovich, M. Levy-Sakin, A. Grunwald, Y. Liebes-Peer, M. Bachar, L. Buzhansky, E. Mossou, V. T. Forsyth, T. Schwartz, Y. Ebenstein, F. Frolow, L. J. W. Shimon, F. Patolsky and E. Gazit, Nat. Nanotechnol., 2015, 10, 353-360.
3 B. Apter, N. Lapshina, A. Handelman, B. D. Fainberg and G. Rosenman, Small, 2018, 14, 1801147.
4 K. Ariga, M. Nishikawa, T. Mori, J. Takeya, L. K. Shrestha and J. P. Hill, Sci. Technol. Adv. Mater., 2019, 20, 51-95.

5 M. N. Nasir, E. Benichou, C. Loison, I. Russier-Antoine, F. Besson and P.-F. Brevet, Phys. Chem. Chem. Phys., 2013, 15, 19919-19924.
6 G. Matar, J. Duboisset, E. Benichou, G. Bachelier, I. RussierAntoine, C. Jonin, D. Ficheux, P.-F. Brevet and F. Besson, Chem. Phys. Lett., 2010, 500, 161-166.
7 A. Handelman, S. Lavrov, A. Kudryavtsev, A. Khatchatouriants, Y. Rosenberg, E. Mishina and G. Rosenman, Adv. Opt. Mater., 2013, 1, 875-884.
8 S. K. Nandi, S. Roy, B. Pal and D. Haldar, Phys. Chem. Chem. Phys., 2023, 25, 5849-5856.
9 M. R. Ghadiri, Adv. Mater., 1995, 7, 675-677.
10 S. Gilead and E. Gazit, Supramol. Chem., 2005, 17, 87-92.
11 C. Gorbitz, Acta Crystallogr., Sect. B: Struct. Sci., Cryst. Eng. Mater., 2018, 74, 311-318.
12 C. H. Gorbitz, Chem. - Eur. J., 2001, 7, 5153-5159.
13 J. Kim, T. H. Han, Y. I. Kim, J. S. Park, J. Choi, D. C. Churchill, S. O. Kim and H. Ihee, Adv. Mater., 2010, 22, 583-587.
14 Q. Li, Y. Jia, L. Dai, Y. Yang and J. Li, ACS Nano, 2015, 9, 2689-2695.
15 B. Akdim, R. Pachter and R. R. Naik, Appl. Phys. Lett., 2015, 106(18), 183707.
16 N. Kol, L. Adler-Abramovich, D. Barlam, R. Z. Shneck, E. Gazit and I. Rousso, Nano Lett., 2005, 5, 1343-1346.
17 D. Isakov, E. de Matos Gomes, M. S. Belsley, B. Almeida and N. Cerca, Nanoscale, 2012, 4, 4978-4982.

18 L. Adler-Abramovich and E. Gazit, Chem. Soc. Rev., 2014, 43, 6881-6893.
19 A. R. Allafchian, E. Moini and S. Z. Mirahmadi-Zare, IEEE Sens. J., 2018, 18, 8979-8985.
20 T. Cipriano, G. Knotts, A. Laudari, R. C. Bianchi, W. A. Alves and S. Guha, ACS Appl. Mater. Interfaces, 2014, 6, 21408-21415.
21 L. Adler-Abramovich and E. Gazit, J. Pept. Sci., 2008, 14, 217-223.
22 L. Adler-Abramovich, N. Kol, I. Yanai, D. Barlam, R. Z. Shneck, E. Gazit and I. Rousso, Angew. Chem., Int. Ed., 2010, 49, 9939-9942.
23 R. M. F. Baptista, P. E. Lopes, A. R. O. Rodrigues, N. Cerca, M. S. Belsley and E. de Matos Gomes, Mater. Adv., 2022, 3, 2934-2944.
24 K. Tao, Z. Fan, L. Sun, P. Makam, Z. Tian, M. Ruegsegger, S. Shaham-Niv, D. Hansford, R. Aizen, Z. Pan, S. Galster, J. Ma, F. Yuan, M. Si, S. Qu, M. Zhang, E. Gazit and J. Li, Nat. Commun., 2018, 9, 3217.
25 N. Amdursky, M. Molotskii, D. Aronov, L. Adler-Abramovich, E. Gazit and G. Rosenman, Nano Lett., 2009, 9, 3111-3115.

26 R. M. F. Baptista, E. de Matos Gomes, M. M. M. Raposo, S. P. G. Costa, P. E. Lopes, B. Almeida and M. S. Belsley, Nanoscale Adv., 2019, 1, 4339-4346.
27 M. Wang, S. Xiong, X. Wu and P. K. Chu, Small, 2011, 7, 2801-2807.
28 N. Amdursky, M. Molotskii, E. Gazit and G. Rosenman, J. Am. Chem. Soc., 2010, 132, 15632-15636.

29 Bruker, APEX4, Bruker AXS Inc., Madison, USA, 2021, V2021.10-0.

30 Bruker, SAINT, Bruker AXS Inc., Madison, USA, 2012, v8.30A.
31 L. Krause, R. Herbst-Irmer, G. M. Sheldrick and D. Stalke, J. Appl. Crystallogr., 2015, 48, 3-10.

32 G. M. Sheldrick, Acta Crystallogr., Sect. C: Struct. Chem., 2015, 71, 3-8.
33 O. V. Dolomanov, L. J. Bourhis, R. J. Gildea, J. A. K. Howard and H. Puschmann, J. Appl. Crystallogr., 2009, 42, 339-341.
34 C. F. Macrae, I. Sovago, S. J. Cottrell, P. T. A. Galek, P. McCabe, E. Pidcock, M. Platings, G. P. Shields, J. S. Stevens, M. Towler and P. A. Wood, J. Appl. Crystallogr., 2020, 53, 226-235.
35 A. L. Spek, Acta Crystallogr., Sect. D: Biol. Crystallogr., 2009, 65, 148-155.
36 D. Kratzert, V104 Available online: https://dkratzert.de/ finalcif.html, (accessed on 20 April 2024).
37 R. M. F. Baptista, C. S. B. Gomes, B. Silva, J. Oliveira, B. Almeida, C. Castro, P. V. Rodrigues, A. Machado, R. B. Freitas, M. J. L. F. Rodrigues, E. de Matos Gomes and M. Belsley, Materials, 2023, 16, 3690.
38 I. J. Bruno, J. C. Cole, M. Kessler, J. Luo, W. D. Motherwell, L. H. Purkis, B. R. Smith, R. Taylor, R. I. Cooper, S. E. Harris
and A. G. Orpen, J. Chem. Inf. Comput. Sci., 2004, 44, 2133-2144.
39 P. R. Spackman, M. J. Turner, J. J. McKinnon, S. K. Wolff, D. J. Grimwood, D. Jayatilaka and M. A. Spackman, J. Appl. Crystallogr., 2021, 54, 1006-1011.
40 J. d. C. Fonseca, J. C. Tenorio Clavijo, N. Alvarez, J. Ellena and A. P. Ayala, Cryst. Growth Des., 2018, 18, 3441-3448.
41 Y. Santiago de Oliveira, W. Saraiva Costa, P. Ferreira Borges, M. Silmara Alves de Santana and A. P. Ayala, Acta Crystallogr., Sect. C: Struct. Chem., 2019, 75, 483-495.
42 M. A. Spackman and D. Jayatilaka, CrystEngComm, 2009, 11, 19-32.
43 M. Delfino, J. Biol. Phys., 1978, 6, 105-117.
44 J. F. Nye, Physical properties of crystals: their representation by tensors and matrices, Clarendon press, Oxford, Repr. paperback ed. edn., 2004.
45 C. R. Bernardo, R. M. F. Baptista, E. de Matos Gomes, P. E. Lopes, M. M. M. Raposo, S. P. G. Costa and M. S. Belsley, Nanoscale Adv., 2020, 2, 1206-1213.
46 P. Kaatz and D. P. Shelton, J. Chem. Phys., 1996, 105, 3918-3929.
47 H. Reis, J. Chem. Phys., 2006, 125, 014506.

---

[a] Centre of Physics of Minho and Porto Universities (CF-UM-UP), Laboratory of Physics for Materials and Emergent Technologies (LaPMET), University of Minho, Campus de Gualtar, 4710-057 Braga, Portugal.
E-mail: rosa_batista@fisica.uminho.pt
[b] Departamento de Física, Universidade Federal do Ceará, Fortaleza, CE 65455900, Brazil
[c] Institute for Polymers and Composites, University of Minho, Campus de Azurém, 4800-058 Guimarães, Portugal

† Electronic supplementary information (ESI) available: S1: crystal data; Table S1.1: atomic coordinates; Table S1.2: anisotropic displacement parameters; Table S1.3: bond lengths and angles; Table S1.4: torsion angles; S2: SHG. CCDC 2391827. For ESI and crystallographic data in CIF or other electronic format see DOI: https://doi.org/10.1039/d5ce00134j